



**HAL**  
open science

## Characterization of the cloud microphysical and optical properties and aerosol-cloud interaction in the Arctic from in situ ground-based measurements during the CLIMSLIP-NyA campaign, Svalbard

Gwenno  Guyot, Frans Olofson, Peter Tunved, Christophe Gourbeyre, Guy Fevbre, Regis Dupuy, Christophe Bernard, G rard Ancellet, Kathy S. Law, Boris Quennehen, et al.

### ► To cite this version:

Gwenno  Guyot, Frans Olofson, Peter Tunved, Christophe Gourbeyre, Guy Fevbre, et al.. Characterization of the cloud microphysical and optical properties and aerosol-cloud interaction in the Arctic from in situ ground-based measurements during the CLIMSLIP-NyA campaign, Svalbard. 2019. insu-01627782

**HAL Id: insu-01627782**

**<https://insu.hal.science/insu-01627782>**

Preprint submitted on 28 Mar 2019

**HAL** is a multi-disciplinary open access archive for the deposit and dissemination of scientific research documents, whether they are published or not. The documents may come from teaching and research institutions in France or abroad, or from public or private research centers.

L'archive ouverte pluridisciplinaire **HAL**, est destin e au d p t et   la diffusion de documents scientifiques de niveau recherche, publi s ou non,  manant des  tablissements d'enseignement et de recherche fran ais ou  trangers, des laboratoires publics ou priv s.



1        **Characterization of the cloud microphysical and optical**  
2        **properties and aerosol-cloud interaction in the Arctic from**  
3        **in situ ground-based measurements during the CLIMSLIP-**  
4        **NyA campaign, Svalbard**

5  
6  
7        Gwennolé GUYOT<sup>1</sup>, Frans OLOFSON<sup>1</sup>, Peter TUNVED<sup>2</sup>, Christophe GOURBEYRE<sup>1</sup>, Guy  
8        FEVBRE<sup>1</sup>, Régis DUPUY<sup>1</sup>, Christophe BERNARD<sup>1</sup>, Gérard ANCELLET<sup>3</sup>, Kathy LAW<sup>3</sup>,  
9        Boris QUENNEHEN<sup>4</sup>, Alfons SCHWARZENBOECK<sup>1</sup>, Kostas ELEFThERIADIS<sup>5</sup>, Olivier  
10        JOURDAN<sup>1</sup>

11  
12        <sup>1</sup> Laboratoire de Météorologie Physique (LaMP), Université Blaise Pascal (UBP), OPGC,  
13        CNRS UMR 6016, Clermont-Ferrand, France

14        <sup>2</sup> Department of Applied Environmental Science (ITM), Stockholm University, Stockholm,  
15        Sweden

16        <sup>3</sup> Laboratoire Atmosphère, Milieux et Observations Spatiales (LATMOS), IPSL, UPMC,  
17        CNRS UMR 8190, Paris

18        <sup>4</sup> Laboratoire de Glaciologie et Géophysique de l'Environnement (LGGE), Université  
19        Grenoble Alpes/CNRS, 38041 Grenoble, France

20        <sup>5</sup> Environmental Radioactivity Laboratory, Institute of Nuclear and Radiological Science &  
21        Technology, Energy & Safety, Attiki, Greece

22  
23        **Abstract**

24  
25        This study will focus on cloud microphysical and optical characterization of three different  
26        types of episodes encountered during the ground based CLIMSLIP-NyA campaign performed  
27        in Ny-Alesund, Svalbard: the Mixed Phase Cloud (MPC), snow precipitation and Blowing  
28        Snow (BS) events. These in situ cloud measurements will be combined with aerosol  
29        measurements and air mass backtrajectory simulations to qualify and parameterize the arctic  
30        aerosol cloud interaction and to assess the influence of anthropogenic pollution transported into  
31        the Arctic.

32        The results show a cloud bimodal distribution with the droplet mode at 10  $\mu\text{m}$  and the crystal  
33        mode centered at 250  $\mu\text{m}$ , for the MPC cases. The precipitation cases presents a crystal  
34        distribution centered around 350  $\mu\text{m}$  with mostly of dendritic shape. The BS cases show a  
35        higher concentration but smaller crystals, centered between 150 and 200  $\mu\text{m}$ , with mainly  
36        irregular crystals.

37        A “polluted” case, where aerosol properties are influenced by anthropogenic emission from  
38        Europe and East Asia, was compared to a “clean” case with local aerosol sources. These  
39        anthropogenic emissions seem to cause higher Black Carbon, aerosol and droplet  
40        concentrations, a more pronounced accumulation mode, smaller droplet sizes and a higher  
41        activation fraction  $F_a$ . Moreover, the activation diameter decreases as the droplet diameter  
42        increases and  $F_a$  increases showing that smaller particles are activated and droplets grow when  
43        the aerosol number decreases. This is in agreement with the first (Twomey) and second  
44        (Albrecht) aerosol indirect effect. The quantification of the variations of droplet concentration  
45        and size leads to  $IE$  (Indirect Effect) and  $NE$  (Nucleation Efficiency) coefficients values around  
46        0.2 and 0.43, respectively. These values are close to those found by other studies in the arctic



47 region which confirms these parameterizations of arctic aerosol-cloud interaction in climate  
48 models.

## 49 **1 Introduction**

50

51 The Arctic is a region where the surface warming is faster than the global average warming,  
52 associated with, in particular, a rapid melting of the sea ice in summer (Vaughan et al., 2013).  
53 This is the so-called arctic amplification. Several studies indicate that the arctic warming is  
54 mainly of anthropogenic origin (e.g., Mc Guire et al., 2006, Serreze and Francis, 2006). The  
55 arctic amplification is due to several positive feedbacks specific to the Arctic, the most  
56 important being the sea ice melting feedbacks (Screen and Simmonds, 2010). Changes in  
57 atmospheric and oceanic circulation, cloud properties (especially cloud cover) and atmospheric  
58 water vapor amount are highly expected but their quantification remains uncertain. Specially,  
59 the effects of clouds dominate the intermodal standard deviation of a temperature rise due to an  
60 increase of atmospheric CO<sub>2</sub> concentration (Dufresne and Bony, 2008).

61

62 Recent remote sensing studies have shown that the clean and stable arctic atmosphere is  
63 characterized by a high occurrence of mixed phase clouds (MPC) all year long, except in winter  
64 and early spring when ice clouds are important (Mioche et al., 2015). However, the Svalbard  
65 region is an exception where MPC are the most frequent cloud independent of season (Mioche  
66 et al., 2015). Moreover, the altitude of the MPC is highly dependent of the height of the  
67 inversion layer. The frequently occurring situation with a stable atmosphere and the low level  
68 pronounced inversion layer promotes low level clouds of stratus form (Curry et al., 1996). The  
69 arctic MPC are composed of a liquid layer on top and below which is located the mixed phase  
70 where ice crystals take form (Gayet et al., 2009). If the crystals grow enough, a precipitation  
71 layer is produced below the cloud. The dynamics together with possible surface coupling and  
72 advection are essential to maintain the MPC during several days (Morrison et al., 2012). This  
73 structure results from a complex network of interactions between numerous local and larger  
74 scale processes that complicates the understanding of the MPC properties evolution and its  
75 impact on arctic climate (Morrison et al., 2012). In the Arctic, the umbrella effect is not  
76 necessarily dominant compared to the cloud greenhouse effect (Quinn et al., 2008), which  
77 suspects that clouds play an important role in the arctic amplification. Several studies have  
78 revealed that MPCs have a large impact on the surface radiative flux in the Arctic (e.g. Kay et  
79 al., 2012, Wendisch et al., 2013).

80

81 Arctic cloud properties are linked to aerosol properties since they can act as Cloud  
82 Condensation Nuclei (CCN) or Ice Nuclei (IN). Thus, aerosol seasonal variability and transport  
83 from lower latitudes play a role in cloud properties evolution. Studies have shown an arctic  
84 annual mean aerosol concentration half that for mid-latitudes. The stable atmosphere and the  
85 dark winter promote growth by coagulation/coalescence of the particles, i.e. an increase in size  
86 and decrease in concentration, with dominant accumulation mode (Tunved et al., 2013). When  
87 the sun rises during spring, these big particles, which can come from lower latitudes, generate  
88 the arctic haze phenomenon (Quinn et al. 2007). The stronger sun light gives rise to increasing  
89 photochemical activity associated with new particle formation and a dominant Aitken mode  
90 (Engwall et al., 2008). Moreover, the ice melting exposes land surfaces that can act as aerosol  
91 sources. Therefore, the aerosol concentration increases until its maximum in summer. These  
92 features were observed in Alaska (Quinn et al., 2002) and Svalbard (Tunved et al., 2013),  
93 proving that they are representatives of the aerosol properties evolution in the Arctic.

94



95 The rapid change in aerosol properties occurring in spring is known to cause changes in arctic  
96 cloud properties, the so-called aerosol indirect effect. Increase in aerosol concentration with  
97 constant Liquid Water Path (*LWP*) is known to increase cloud droplet concentration and cloud  
98 optical thickness but decrease droplet size (Twomey, 1974, 1977), decrease the precipitation  
99 efficiency and increase the cloud lifetime (Albrecht, 1989). Also, in a temperature rise scenario,  
100 the cloud height is expected to increase (Pincus and Baker, 1994). The impacts of anthropogenic  
101 aerosol transported to the Arctic on clouds are not fully understood, but Garrett and Zhao (2006)  
102 showed that the cloud emissivity is higher for polluted case, contributing to the arctic warming.  
103

104 In the case of arctic MPC where liquid and ice phases coexist, the aerosol-cloud interaction is  
105 complexified by the addition of the ice phase and several interaction mechanisms have been  
106 assumed. Lohmann (2002a, 2002b) proposed that an increase in ice nuclei could increase the  
107 cloud ice content at the expense of the liquid content. This so-called glaciation indirect effect  
108 would mean, as the precipitation is more efficient for the ice phase, a decrease in cloud cover  
109 in lifetime. The riming indirect effect predicts a riming efficiency decrease due to the  
110 supercooled droplet size decrease. Thus, an increase in Cloud Condensation Nuclei (CCN)  
111 could lead to a decrease in Ice Water Content (IWC) and ice particles concentration (Borys et  
112 al., 2003). According to the data of the two measurement campaigns ISDAC (Indirect and Semi-  
113 Direct Aerosol Campaign) and MPACE (Mixed-Phase Arctic Cloud Experiments), Jackson et al.  
114 (2012) found a correlation corresponding to the glaciation effect above the cloud liquid phase  
115 but no evidence of the riming effect. Mc Farquhar et al. (2011) showed that the aerosol size is  
116 the main parameter to explain the particles activation and that the chemical properties don't  
117 determine the ability of an aerosol to act as a CCN, i.e. the Kelvin effect is dominant compared  
118 to the Raoult effect in the Arctic.  
119

120 The work presented here is included in the frame of the project CLIMSLIP (CLimate IMpacts  
121 of Short-Lived Pollutants in the polar region). The main objective of this project is to reduce the  
122 uncertainties of the radiative forcing due to the anthropogenic emissions of tropospheric ozone,  
123 methane and aerosol including Black Carbon (BC). This article will focus on the arctic ground  
124 based in situ cloud and aerosol measurement study, performed at the Mount Zeppelin station  
125 (474 meters altitude), in Ny-Alesund, Svalbard, performed during spring 2012. First, a  
126 classification and characterization of the different types of cases will be presented. Then, a  
127 comparison between a polluted and a clean case will be made, based on air masses  
128 backtrajectories. In the end, the different aerosol-cloud interactions will be discussed and, if  
129 possible, quantified.  
130

## 131 **2 Site & instrumentation**

132

### 133 **2.1 Site**

134

135 The campaign was carried out between February 26 and May 2 at the Mount Zeppelin station  
136 (78°56'N, 11°53'E) located south-west of the Ny-Alesund village, Svalbard, at an altitude of 474  
137 meters above sea level. This station presented in Figure 1 was built and is managed by the  
138 Norwegian Institute for Air Research (NILU). The Zeppelin observatory is mostly unaffected by  
139 local sources and is considered to be within the boundary layer most of the time (Tunved et al.,  
140 2013). This station represents remote arctic conditions and is a part of the European observation  
141 network ACTRIS (Aerosols, Clouds, and Trace gases Research InfraStructure network).  
142 Continuous measurements of atmospheric trace gases and aerosol physical and chemical properties



143 are performed all year long. The station is also equipped with instruments to measure temperature,  
144 humidity and wind speed and direction.  
145 A ceilometer, CL51 model, was installed in the Ny-Alesund village at sea level. This remote  
146 sensing instrument is designed to measure the clouds within an altitude range between 0 and 15  
147 km. It uses the technology of a lidar with a laser wavelength at 910 nm. During CLIMSLIP, the  
148 ceilometer was used to retrieve the approximate altitude of the mixed phase and the liquid layers  
149 and showed good agreement with the microphysical measurements. However, in some cases,  
150 fog or an optically thick ice layer prevents the laser beam from penetrating within the cloud  
151 system.  
152  
153



154 Figure 1: Picture of the Mount Zeppelin station ([www.npolar.no](http://www.npolar.no))  
155  
156

## 157 2.2 Instrumentation and data processing

158

### 159 2.2.1 Cloud instrumentation

160

161 The cloud ground based instrumentation used during CLIMSLIP-NyA was installed on a  
162 measurement pole and is presented in Figure 2. The cloud optical and microphysical properties  
163 were thus assessed by three independent instruments: a PMS Forward Scattering Spectrometer  
164 Probe (FSSP-100), a Cloud Particle Imager (CPI) and a Polar Nephelometer (PN). They were  
165 all connected to the same pump by plastic tubes, leading to the sampling volume indicated on  
166 Figure 2. They were operated approximately 2 m above the platform level and mounted on a  
167 tilting and rotating mast, allowing them to be moved manually in the prevailing wind direction.  
168 The proper alignment of their inlet with the flow was based on the wind direction measurements  
169 performed by a mechanical and ultrasonic anemometer.

170

171 The FSSP-100 measures the number and the size of particles going through the sampling  
172 volume, from the forward scattering of a 632.8 nm wavelength laser beam (Knollenberg, 1981,  
173 Dye and Baumgardner, 1984). Using the Mie theory, this instrument is dedicated to droplets.  
174 The Particle Size Distribution (PSD) is thus computed in 15 adjustable size classes with  
175 uncertainties on the effective diameter and *LWC* of respectively 2  $\mu\text{m}$  and 30 % (Febvre et al.,  
176 2012).

177 The CPI is an imager and takes pictures of the particles when going through the detection  
178 volume with 256 grey levels, thanks to a CCD camera with a resolution of  $1024 \times 1024$  pixels.  
179 These images allow computing the particles size and so the PSD, but several morphological



180 parameters are also retrieved and are used to classify the sampled particle in 10 shape  
181 categories: spheroid, needle, column, plate, bullet, stellar, graupel, rosette, sideplane and  
182 irregular (Lefèvre, 2007). However, a manual classification has been done during the  
183 CLIMSLIP campaign due to some malfunctions of the automatic classification. The  
184 determination of the IWC is realized according to the Baker and Lawson (2006) and Lawson  
185 and Baker (2006) method. The uncertainties on the concentration and the effective diameter are  
186 assessed respectively as 50 % and 80 %.

187 The PN measures the scattering phase function of a set of cloud particles thanks to a 804 nm  
188 wavelength laser beam and 56 photodiodes distributed over scattering angles between 3.5° and  
189 172.5° (Gayet et al., 1997). From the scattering phase function can be computed two important  
190 integrated optical parameters, the extinction coefficient and the asymmetry parameter with  
191 accuracies estimated within 25% and 4%, respectively (Gayet et al., 2002).

192 The Nevzorov probe is a hot wire device at constant temperature with two captors and an  
193 electrical resistor. The particles are vaporized, and an electrical power is provided to the  
194 resistor. The resulting power is related to the *LWC* and *TWC*, depending on the captor  
195 (Korolev et al., 1998). Due to high discrepancies, this instrument was used only for instrumental  
196 comparison and data processing analysis and will not be discussed further.

197



198

199 Figure 2: Cloud instrumentation used during CLIMSLIP. Indicated are: particle size range,  
200 main cloud properties measured and theoretical sampling speed.

201

202

### 203 2.2.2 Aerosol instrumentation

204

205 The particle inlet at the Mount Zeppelin station is a Whole Air Inlet, which possesses a heating  
206 system that prevents the inlet to be filled by ice or frost and to evaporate the condensed water  
207 or ice. Thus, all the aerosols (CCN, IN or interstitial) are sampled by the instruments described  
208 hereafter. The aerosol sampling covers particles sizes between 3 and 809 nm (Tunved et al.,  
209 2013).

210

211 The Mount Zeppelin aerosol instrumentation is composed of one Condensation Particle Counter  
212 (CPC), one Differential Mobility Particle Sizer (DMPS), one aethalometer and one aerosol  
213 nephelometer, which are running continuously throughout the year. The CPC, 3015A model, is  
214 a particle counter for aerosol diameters larger than 3 nm. It measures aerosol concentration up  
215 to 10<sup>5</sup> particles/cm<sup>3</sup> with an accuracy of 10 % (TSI, 2002). The DMPS is a CPC combined with  
216 a Differential Mobility Analyzer (DMA), which allows selecting different size ranges. The  
217 aerosol PSD is obtained with 22 diameter classes going from 25 to 809 nm. The aethalometer  
218 assesses the Black Carbon (BC) concentration based to the optical extinction of the aerosols



219 collected on a filter (see Eleftheriadis et al., 2009, for details). The nephelometer measures the  
220 aerosol scattering coefficient for three wavelength: 450, 550 and 700 nm (TSI, 2005). During  
221 CLIMSLIP, this nephelometer was used with a time resolution of 5 minutes.

222

### 223 2.2.3 Data processing

224

225 The three cloud instruments operated at a one Hz resolution. The data processing has followed  
226 the conclusions of the cloud instrumentation study presented in Guyot et al. (2015). This paper  
227 highlights the biases that can exist between the instruments and the need of an Ensemble of  
228 Particles Probe (EPP) to standardize the data. In the case of the CLIMSLIP campaign, such  
229 correction was not possible for two reasons not developed further. (1) Strong discrepancies of  
230 the EPP Nezhvorov probe, probably because of a too low sampling speed. (2) The  
231 standardization according to the extinction coefficient of the PN is not consistent with the  
232 aerosol data (there are more droplets than CCN). Thus, this study will not provide quantitative  
233 results but qualitative ones based on case comparisons and variation studies.

234 According to Guyot et al. (2015), measurements with an angle between the instruments  
235 orientation and the wind direction higher than 30° can modify the PSD due to changes in the  
236 sampling conditions. Those measurements were therefore not taken into account for the study.  
237 Moreover, the ground based low sampling speed induces low sampling rate, especially for the  
238 CPI with values between 0.5 and 20 sampled particles per minute. This doesn't allow us to  
239 work on low time resolution scale. To get sufficient particle statistics, the minimum average  
240 time resolution will be 1 minute for the FSSP and one day for the CPI.

241

242 During the aircraft campaign, a cloud particle can break on impaction with the inlet due to the  
243 high sampling speed corresponding to the plane speed. This results in more numerous and  
244 smaller droplets or crystals and creates artifacts in the PSD (Rogers et al., 2006). Due to the  
245 low sampling speed, ground based measurements has the advantage to avoid this effect, but at  
246 the expense of the sampling rate.

247

248

## 249 **3 Identification and characterization of the study cases**

250

### 251 **3.1 Overview**

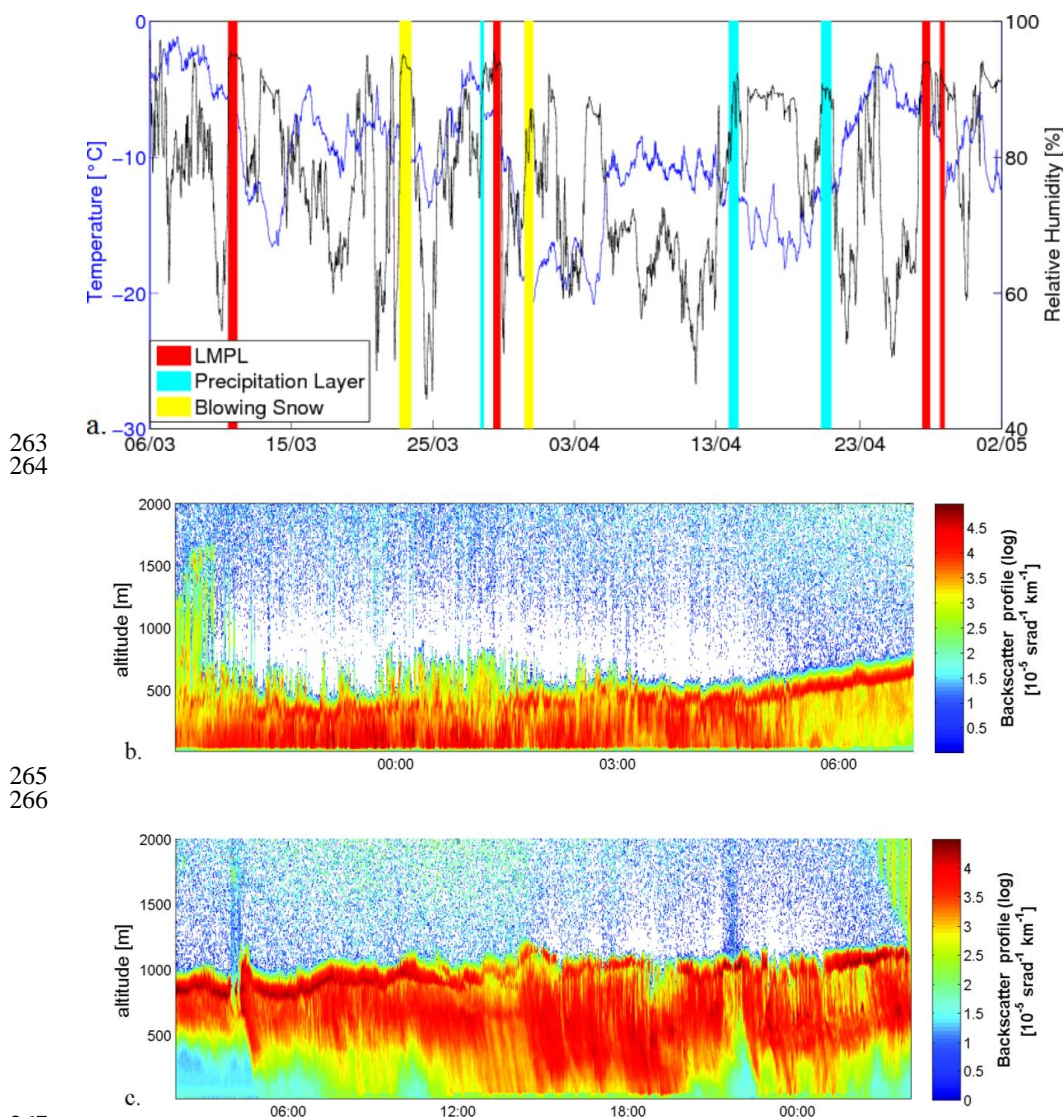
252

253

254 Several kinds of episodes were met during CLIMSLIP. Figure 3.a shows those episodes with  
255 the time series of measured temperature and relative humidity. Thus, according to the  
256 ceilometer measurements and observations, we enumerate:

- 257 - 4 episodes of sampling of the liquid and mixed phase layer (LMPL) of MPC, on March  
258 11<sup>th</sup> and 29<sup>th</sup> and April 27<sup>th</sup> and 28<sup>th</sup>.
- 259 - 3 cases of sampling of the precipitation layer of MPC, on March 28<sup>th</sup> and April 14<sup>th</sup> and  
260 20<sup>th</sup>.
- 261 - 2 occurrences of Blowing Snow (BS), on March 23<sup>th</sup> and 31<sup>th</sup>.

262



263  
264

265  
266

267  
268

269 Figure 3: a) Time series of the temperature and relative humidity measured at the Zeppelin  
270 station. The different cases are plotted with colored columns. Examples of time series of the  
271 ceilometer attenuated backscattered coefficient profile in  $\text{km}^{-1} \text{ sr}^{-1}$  for b) MPC case (April  
272 27<sup>th</sup>) and c) precipitation case (April 14<sup>th</sup>).

273

274 The cases called “LMPL” and “Precipitation layer” both reveal the presence of a MPC, i.e.  
275 where cloud in situ instrumentation sampled ice and/or liquid particles. But, in the first case,  
276 the ceilometer shows the liquid layer around 500 meters altitude (Figure 3.b). This liquid layer  
277 having a very strong extinction coefficient, the ceilometer beam does not go through, what  
278 happens above the liquid layer is therefore unknown. On the same time, droplets are sampled  
279 by the FSSP. Following the altitude of the cloud, the station is in the liquid layer or the mixed  
280 phase layer. These episodes are characterized by relative humidity maximum.





281 In the second case, the ceilometer locates the liquid layer around 1 km altitude or more (Figure  
282 3.c). No droplets are sampled. The station is so below the mixed layer, within the ice  
283 precipitation. This layer has a variable extinction coefficient depending on the crystal density  
284 but the laser beam is not completely attenuated. The relative humidity shows high values around  
285 90 % but remains lower than the MPC cases.

286 Moreover, the temperature varied between -20 to -1 °C, so it remains always below the  
287 solidification point, liquid particles were always supercooled droplets. The Blowing Snow  
288 episodes will be discussed in annex.

289

290 In the following, the LMPL and precipitation layer cases will be microphysically and optically  
291 characterized. These characterizations will be useful to determine futures measurements that  
292 are not completed with visual observations (e.g., remote sensing measurements). Moreover,  
293 combined with other measurement campaign in the Arctic, we hope to increase knowledge  
294 about growth processes in low level mixed phase arctic clouds.

295

296

### 297 **3.2 Characterization of the LMPL cases**

298

299 Arctic MPC can be characterized by a succession of layers with liquid or ice dominance. The  
300 phase heterogeneity is both horizontal and vertical. Because of the fixed position of the  
301 measuring station, we could not control the location of the measurements within the cloud  
302 system. However, a characterization of the mean parameters is possible.

303

304 The determination of the thermodynamic phase of a cloud can be based on microphysical and  
305 optical criteria. Figure 4 presents the occurrence number of the MPC liquid fraction  $F_{liq}$  and the  
306 asymmetry parameter  $g$ .  $F_{liq}$  is computed as :

307

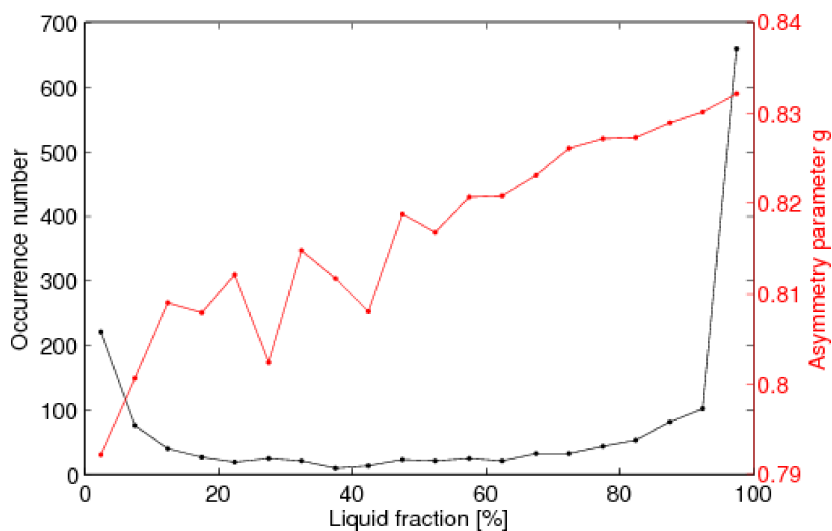
$$308 \quad F_{liq} = \frac{LWC_{FSSP}}{(LWC_{FSSP} + IWC_{CPI})} \quad (1)$$

309

310 The results show a higher observation frequency for extreme  $F_{liq}$  values (close to 0 or 100 %).  
311 The minimum frequency is between 20 and 70 %. This means that the low level mixed phase  
312 cloud layers are preferentially with liquid or ice dominance for the spatial resolution of our  
313 measurements. This confirms the conclusions from the scientific literature (e.g., Gayet and al.,  
314 2009; Korolev and Isaac, 2006).

315 Moreover,  $g$  shows a more or less linear relation with  $F_{liq}$ . This highlights the relation between  
316 the optical properties and the microphysical properties. Therefore, the knowledge of the MPC  
317 microphysical properties is a key parameter to reliably assess the radiative transfer in the Arctic.  
318 The  $g$  variability is significantly larger for  $F_{liq}$  below 50 %. This tends to show a more complex  
319 optical behavior for ice dominating layers.

320



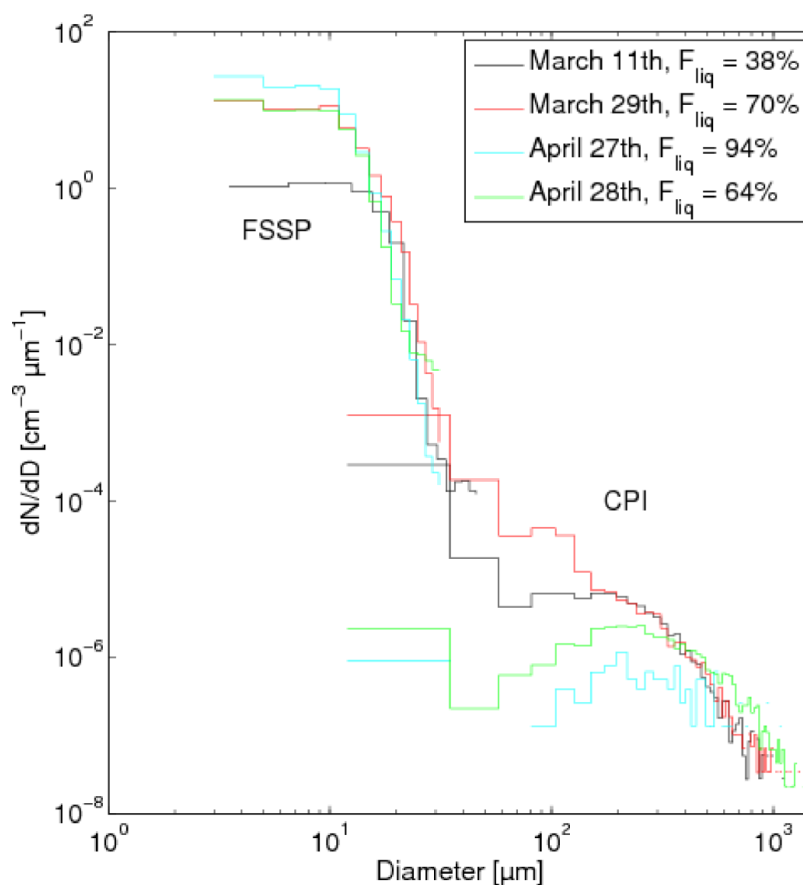
321  
322 Figure 4: Occurrence number and mean values of  $g$  in relation to the liquid fraction  $F_{liq}$  for the  
323 four LMPL cases.  $F_{liq}$  is derived from the CPI and FSSP measurements (see Eq. 1) with 1  
324 minute resolution corresponding to a spatial resolution of 800 meters.

325  
326  
327 Figure 5 shows the average PSD, from 3  $\mu\text{m}$  to 2.3 mm, obtained with the FSSP and the CPI  
328 for the four LMPL cases. The mean  $F_{liq}$  is also indicated. The four PSD show similar trends,  
329 i.e. two modes centered at 10  $\mu\text{m}$  for droplets and around 250  $\mu\text{m}$  for ice crystals.

330 According to Costa et al. (2014), these PSD correspond to the coexistence regime characterized  
331 by  $RH_w$  (relative humidity according to liquid water) and  $RH_i$  (relative humidity according to  
332 ice)  $> 100\%$  and stable coexistence of crystals and supercooled liquid droplets with the droplet  
333 PSD  $10^6$  higher than the crystal PSD. This is opposite to the Bergeron regime where  $RH_w < 100\%$   
334 and  $RH_i > 100\%$ , so the crystals grow in expense of the droplets (Costa et al., 2014). This  
335 reveals that the Wegener-Bergeron-Findeisen process doesn't alone explain the formation and  
336 growth of ice crystals.

337 However, the March 11<sup>th</sup> and 29<sup>th</sup> PSDs show differences with the other cases with a high  
338 concentration for the smallest CPI classes. This is due to big droplets sampled by the CPI. The  
339 FSSP doesn't show such consequent differences in droplet PSD or diameter. We also point out  
340 that the absolute values should not be taken into account. Indeed, in addition to instrumental  
341 issues (see Guyot et al., 2015), the results and the differences between the cases are largely  
342 dependent on the station residence time within the liquid or mixed layer which cannot be  
343 controlled. Similar PSDs were observed at the Mount-Zeppelin station by Uchiyama et al.  
344 (2013) in 2011. This publication concludes that the liquid/ice distribution is a function of the  
345 cloud evolution stage; we highlight here the importance of the station position inside the cloud  
346 system for our data analysis.

347  
348



349

350

351 Figure 5: Cloud PSD in  $\text{cm}^{-3} \mu\text{m}^{-1}$  measured by the FSSP [3-50  $\mu\text{m}$ ] and the CPI [15-2300

352

353

354

355

356

357

358

359

360

361

362

363

364

365

366

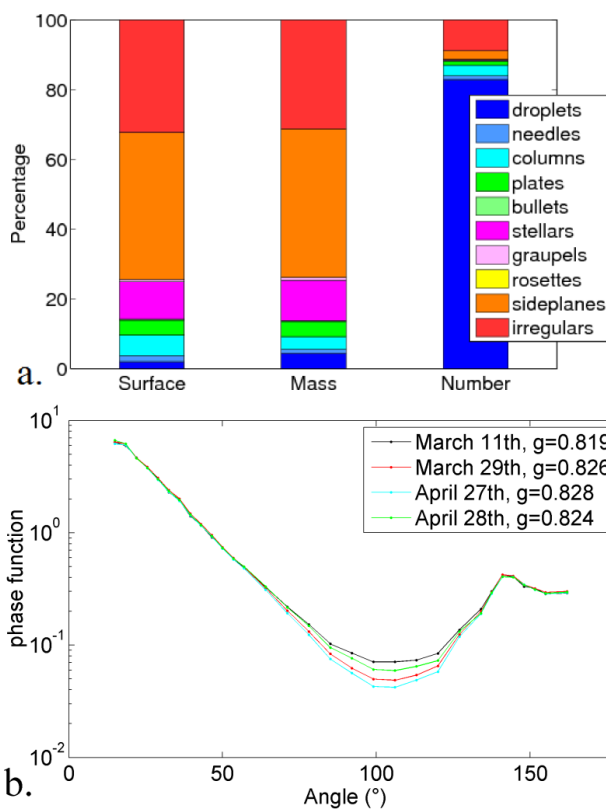
367

The shape classification performed by the CPI is presented Figure 6.a. The high droplet concentrations of the smallest CPI classes observed on March 11<sup>th</sup> and 29<sup>th</sup> (see Figure 5) are responsible of the strong number dominance of the droplets with a value of around 85 %. However, liquid water represents a very small proportion in mass and surface fractions. For these two quantities, side planes and irregular shapes dominate.

The assessment of the crystal growth mode is confronted to the fact that the measurement station can change its position in the cloud. An evolution in the CPI PSD is so not necessary due to particles growth. However, the crystal shape, accurately measured by the CPI, is a good indicator for the growth mode and the high percentage of regular shape would indicate a growth dominated by vapor deposition. Aircraft measurements performed in Svalbard in 2007 show similar results, with in particular strong presence of irregulars and side planes for altitudes and temperatures around 500 m and -12 °C, respectively (Gayet et al., 2009)



368



369

370

371

372

373

374

375

376

377

378

379

380

381

382

383

384

385

386

387

388

389

390

391

Figure 6: a) CPI shape classification in surface, mass and number for the LMPL cases. The color represents the occurrence percentage of the shapes as indicated by caption, and b) average standardized phase functions measured by the PN for the four LMPL cases. Caption indicates the asymmetry parameter.

Measurements of the cloud particle scattering properties performed by the PN allow to study the optical signature of the main microphysical properties observed on the MPC. Figure 6.b displays the average phase functions and asymmetry parameters ( $g$ ) for the four LMPL cases. Differences between the experiments are negligible in forward and backward scattering but within the lateral scattering domain [60°; 130°]. The scattering increases when  $g$  decreases. The 1 minute average  $g$  values during the whole measurement campaign are included between 0.74 and 0.85, which is consistent with results obtained by Garrett et al. (2001).

Combined with Figure 5, these results show that  $g$  and the lateral scattering are related to microphysical properties. Indeed, lateral diffusion increases when  $F_{liq}$  decreases. Therefore, March 11<sup>th</sup> experiment presents the lower  $F_{liq}$  (38 %), the higher lateral scattering and the lower average value of  $g$  (0.819). The contrary is shown in the April 27<sup>th</sup> case ( $F_{liq} = 94\%$ ,  $g = 0.828$ ). This is consistent with previous studies (Gayet et al., 2009; Jourdan et al., 2010) and also proves the qualitative coherence between the FSSP and the PN.

The analysis of the optical-microphysics coupling is limited by the sampling speed and rate and the PN measurement accuracy. Indeed, a mean component analysis failed to establish a relationship between the phase function and the crystal morphology, as highlighted by Jourdan et al. (2010).



### 392 3.3 Characterization of the precipitation cases

393

394 Figure 7 displays the average CPI PSD for the three cases of precipitation. The FSSP is blind  
395 for those particles sizes. The April 14<sup>th</sup> and 20<sup>th</sup> experiments show a PSD with very low  
396 concentrations, close to the detection limit, centered around 350  $\mu\text{m}$  and accompanied by  
397 relatively low temperature  $< -10^\circ\text{C}$ . The March 28<sup>th</sup> case differs from the two other experiments  
398 with higher concentrations and a PSD centered around 200  $\mu\text{m}$ , similar to the LMPL cases.  
399 Besides, the temperature is higher with an average value of  $-5^\circ\text{C}$ . This could reveal an influence  
400 of the mixed layer and/or temperature effect.

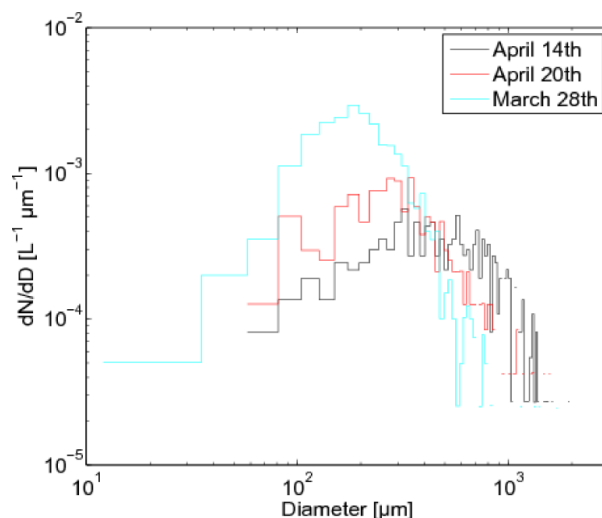
401 However, the ceilometer located the cloud base at an altitude of approximately 1000 m for the  
402 three days, which would indicate that the station position doesn't explain the differences. The  
403 temperature differences could lead to different growth processes and so different sizes.

404 This information can be provided by the CPI image classification presented Figure 8.a showing  
405 a pronounced presence of stellars. Even if the stellar crystals aren't a majority in number, they  
406 stand for more than half of total surface and mass. However, the number shape distribution was  
407 not identical for the three days. Indeed, the 14<sup>th</sup> and 20<sup>th</sup> April experiments are dominated by  
408 stellar whereas the March 28<sup>th</sup> case shows a much more important contribution of plaque,  
409 irregular and needle. As the concentration is 5 times higher for the March 28<sup>th</sup> case, its  
410 contribution in the total number distribution is more important.

411 Therefore, even if the temperature measured at the station is potentially different than the crystal  
412 formation and growth temperatures and the oversaturation according to the ice was not  
413 measured, we have seen that the CPI measurements show that temperatures below  $-10^\circ\text{C}$  are  
414 favorable to the formation of big size crystals such as stellar, whereas, for warmer temperatures,  
415 plaque, irregular and needle crystals with smaller sizes dominate. This agrees with the crystal  
416 classification studied by Bailey and Halley (2009) and explains the differences in the daily PSD.

417

418

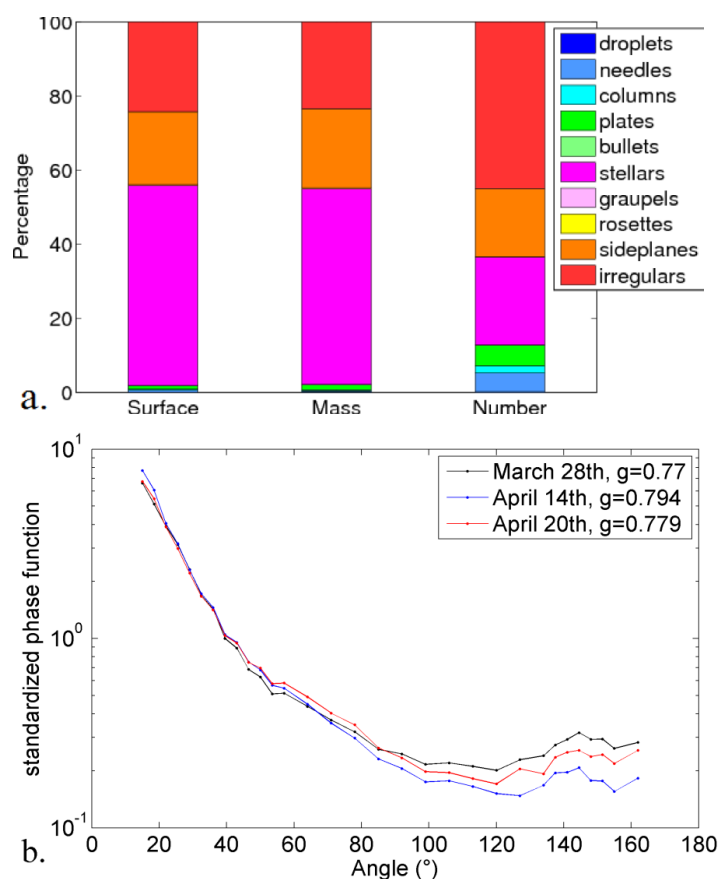


419

420

421

Figure 7: Same as Figure 5 for the precipitation cases.



422

423

424

425

426

427 Figure 8.b presents the average phase functions of the precipitation cases. The lateral scattering  
 428 is more important than for the measurements of the mixed and liquid layers. The asymmetry  
 429 parameter is lower around 0.79 which is typical for ice particles. Notable differences  
 430 are observed for scattering angles as low as 40°. These differences are probably due to the crystal  
 431 morphology variability. Unfortunately, such relationships were not observed with the  
 432 CLIMSLIP data. Indeed, a principal component analysis didn't allow discriminating the phase  
 433 function according to the crystal shape. This can be explained by the low sampling rate during  
 434 the precipitation events involving a very low crystal statistics.

435

436

437 To conclude, the results were limited by the low particle sampling rate and the uncontrolled  
 438 position of the station inside the cloud system. However, differences between LMPL and  
 439 precipitation layer have been explicated and allow a quick recognition without visual  
 440 observations in future studies. These results will be compared to other measurement campaign  
 441 for a better understanding of the microphysical processes and feedbacks that take place in low  
 442 level mixed phase arctic clouds.

443

444



#### 445 **4 Aerosol-cloud interaction in the Arctic**

446

447 The objective of this part is to quantify the effects of the aerosol properties on the cloud  
448 properties observed during the CLIMSLIP campaign. To do this, we will in a first step compare  
449 the two experiments of March 11<sup>th</sup> and 29<sup>th</sup> that will be the “clean” and “polluted” cases,  
450 respectively. In a second step, several aerosol cloud-interaction processes will be evaluated and  
451 in situ measurements will be used to assess quantities that are required in parametrization of the  
452 arctic aerosol-cloud interaction.

453

#### 454 **4.1 Section on tools: the FLEXPART-WRF model and definitions**

455

456 This analysis will be supported by results from the lagrangian particle dispersion model  
457 FLEXPART-WRF (version 3.1, Brioude et al., 2013) adapted from the FLEXPART model  
458 (version 6.2, Stohl et al., 2005). FLEXPART-WRF simulates long distance transport and, in a  
459 mesoscale, the moist and dry scavenging and the diffusion of atmospheric tracers and air masses  
460 (see Stohl et al., 1998, Stohl and Thomson, 1999, or Stohl et al., 2005, for more details). The  
461 FLEXPART-WRF model was driven by WRF (Skamarock et al., 2008) meteorological  
462 forecasts to provide air masses back-trajectories and several tracers’ origins.

463

464 For each single run, 20000 pseudo-particles were released from a small volume surrounding  
465 the analyzed position. Then, they were then tracked backward in time. The model output a  
466 tridimensional distribution of the Potential Emission Sensitivity (PES) on a 1° longitude x 1°  
467 latitude resolution grid. The PES is expressed in s/kg, which corresponds to the residence time  
468 of air particles within a given cell. In order to investigate the potential sources of the pollution  
469 transported to the Arctic and since the pollutants generally remain below the inversion layer,  
470 the model output is integrated over the first kilometer atmospheric column and becomes a  
471 Footprint PES (FPES). Combined with the ECLIPSE (Evaluating the Climate and Air Quality  
472 Impacts of Short-Lived Pollutants, see Klimont et al., 2016) atmospheric pollutants emission  
473 inventory, FLEXPART-WRF provides a valuable insight on the potential geographic  
474 contribution of anthropogenic sources for pollution tracers such as CO, SO<sub>2</sub> and BC. The  
475 combination between the FPES and the emissions is called the Potential Source Contribution  
476 (PSC) expressed in kg of tracer per air kg. In this study, we will focus on the CO tracer which  
477 gives an assessment on the origin of the anthropogenic pollution transported to Svalbard.

478

479 The aerosol cloud interaction study will also be supported by two other parameters: the  
480 activation fraction  $F_a$  and the activation diameter  $D_a$ .  $F_a$  can be defined as the percentage of  
481 aerosols becoming CCN (Abdul-Razzak et al., 1998) and is computed by the ratio of the FSSP  
482 and CPC concentration. The CPC was chosen because it provides the largest aerosol size range:

483

$$484 \quad F_a = \frac{N_{drop}}{N_{aerosol}} = \frac{N_{FSSP}}{N_{CPC}} \quad (2)$$

485

486

487 We define  $D_a$  as the diameter beyond which all the aerosols are activated, assuming the aerosol  
488 chemistry effect is negligible (Abdul-Razzak et al., 1998). During CLIMSLIP,  $D_a$  is calculated  
489 as the DMPS diameter for which the DMPS total concentration is equal to the FSSP  
490 concentration. Even if the aerosol size range is smaller for the DMPS than the CPC, the DMPS  
491 was chosen because the aerosol PSD is necessary:

492



493

$$\sum_{D_{max}}^{D_a} n_{DMPS}(D) = N_{FSSP} \quad (3)$$

494

#### 495 4.1 The “Clean” case of March 11<sup>th</sup>

496

497 The March 11<sup>th</sup> case, just like March 29<sup>th</sup>, presents a stable atmosphere with a low level mixed  
 498 phase cloud. The liquid layer was sampled but, unfortunately, the ceilometer beam was almost  
 499 entirely attenuated within the first 500 meters, avoiding to assess cloud top and base altitude.

500 The sounding balloon show the inversion layer around 925 mb (700 m) for both days.

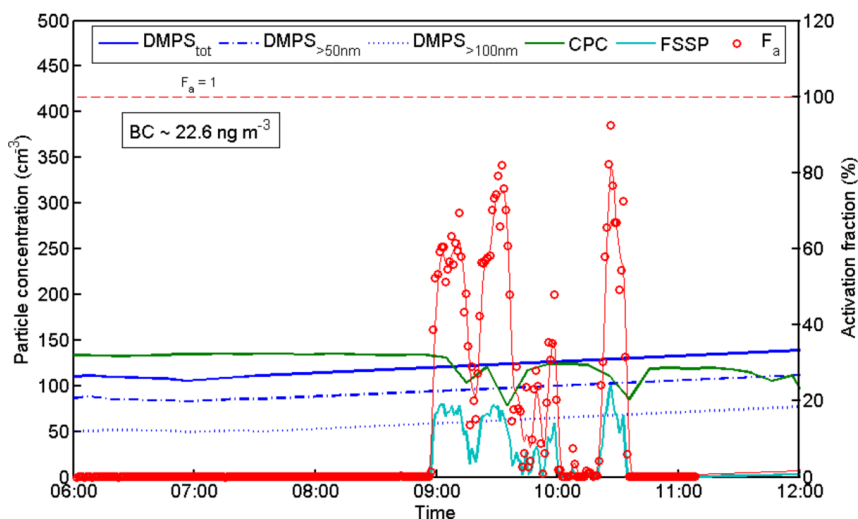
501 Figure 9 shows the time evolution of the DMPS, CPC and FSSP concentration, the activation  
 502 fraction and the average BC concentration. The DMPS ceased to work from 7:30 until the  
 503 following day, but, as the CPC and aethalometer parameters show almost constant values until

504 12:00, the DMPS concentration is assumed to do the same. The DMPS concentration is plotted  
 505 for different particles sizes (total, > 50 nm and > 100 nm). The DMPS PSD shows a bimodal  
 506 distribution with a pronounced Aitken mode which is as important as the accumulation mode  
 507 (not shown). This is obvious in Figure 9 where the accumulation mode concentration, i.e.  
 508 particles sizes larger than 100 nm, equals half the total concentration.

509 The CPC displays an aerosol concentration (> 3 nm) relatively stable and weak between 100  
 510 and 130 cm<sup>-3</sup>. The average BC concentration reaches 22.6 ng m<sup>-3</sup> during the liquid episode. The  
 511 FSSP shows a droplet concentration up to 100 cm<sup>-3</sup>, which leads to  $F_a$  values between 60 and  
 512 80 % for the sections clearly in the densest zone of the MPC liquid layer.

513 The FSSP droplet effective diameter is around 12 μm and the DMPS effective diameter around  
 514 250 μm.  $D_a$  shows very high variations with a mean value around 150 nm (not shown).

515



516

517 Figure 9: Time series of aerosol concentrations measured by the DMPS and the CPC, droplet  
 518 FSSP concentration and the activation fraction, for the March 11<sup>th</sup>. The DMPS concentration  
 519 was divided into three groups: the total concentration [25 - 809 nm], particles larger than 50  
 520 nm [50 - 809 nm] and larger than 100 nm [100 - 809 nm], the latter corresponding to the  
 521 accumulation mode concentration. The activation fraction has been plotted with a sliding average  
 522 of 5 minutes; the average aethalometre BC concentration is indicated.



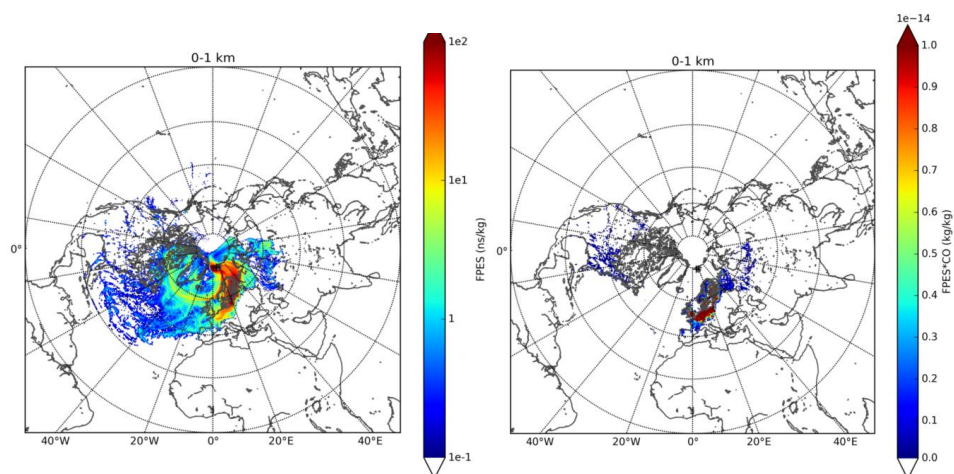


Figure 10: a) FLEXPART-WRF 12 days FPES from the simulation initiated from Mount-Zeppelin on March 11<sup>th</sup> between 9 AM and 12 AM UTC. b) PSC computed from the FPES of Figure a) for the CO, expressed in kg CO per kg air.

523

524

525

526

527

528

529

530

531

532

533

534

535

536

537

538

539

540

541

542

Figures 10 a and b present respectively the FPES over 12 days and the PSC of CO for the air mass arriving at the station during the liquid episode of the March 11<sup>th</sup> described in Figure 9. The FPES shows that the aerosol sources are mainly located in the north of Scandinavia and so that the long-range transport of anthropogenic aerosols is relatively limited. Indeed, over the FLEXPART-WRF time computation of 12 days, the air masses come principally from Svalbard and Scandinavia surrounding, showing very slow move. The CO PSC map presents an anthropogenic origin dominated by North Europa: Scandinavia, north of Germany, Netherland, Belgium and north of France.

The closer air masses origin makes this case the “clean” case. The important contribution of local aerosol sources, mainly composed of gaseous precursors for the arctic region during this period of the year (Quinn et al., 2007), explains the relative small aerosol mean diameter and the high Aitken mode concentration observed by the DMPS (see Figure 9).

543

#### 4.2 The “Polluted” case of March 29<sup>th</sup>

544

545

546

547

548

549

550

551

552

553

554

555

556

Figure 11 displays the same time series as Figure 9 for the liquid episode of March 29<sup>th</sup>. The CPC and DMPS total concentration are decreasing going respectively from 220 cm<sup>-3</sup> to 120 cm<sup>-3</sup> and from 175 cm<sup>-3</sup> to 80 cm<sup>-3</sup>, due to the scavenging by ice precipitation. The FSSP droplet concentrating reaches 150 cm<sup>-3</sup> and the average BC concentration 65.8 ng m<sup>-3</sup>. Comparing to the March 11<sup>th</sup> case, these four concentration are all higher during the March 29<sup>th</sup>. The activation fraction is also higher on March 29<sup>th</sup> with values between 80 and 100 % in the liquid layer and  $F_a$  increases as the aerosol concentration decreases.

Just like March 11<sup>th</sup>,  $D_a$  shows very variable values around 150 nm (not shown). Its high variability makes this parameter unsuitable when comparing the two cases. However,  $D_a$  decreases from around 150 nm to 50 nm and the FSSP effective diameter increases from 8 to 10  $\mu$ m when  $F_a$  increases, proving that smaller aerosol particles are activated and droplets grow when the aerosol number decreases.



557 Moreover, the DMPS PSD shows that 90 % of the aerosol concentration is included in the  
558 accumulation mode, with an effective diameter almost constant at 300 nm. Therefore, the  
559 aerosol diameter is larger and the droplet diameter is smaller for the March 29<sup>th</sup> case compared  
560 to the March 11<sup>th</sup> case.  
561

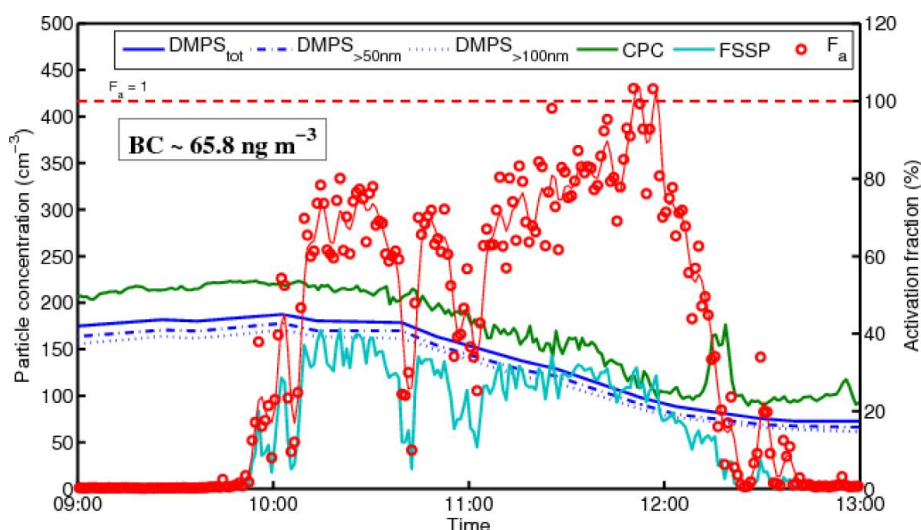


Figure 11: Same as Figure 9 for the March 29<sup>th</sup> case

562  
563  
564

The differences observed between the two days can be explained by the air masses origin. Figure 12 shows the same FLEXPART-WRF FPES and CO PSC for the air mass arriving at the station during the liquid episode of the March 29<sup>th</sup>. Backtrajectories distinguish clearly two origin regions. The first one is Western Europa. The second air mass shows higher values of time residence and comes from northeast Asia: northeast China and extreme east Russia. The particularity of March 29<sup>th</sup> consists thus in this air mass coming from Asia which is the region generally accepted to emit the highest aerosol concentration compared to the others regions of the world (Boucher et al., 2013).

573  
574  
575  
576  
577  
578  
579  
580  
581  
582

Therefore, compared to the “clean” case of March 11<sup>th</sup>, March 29<sup>th</sup> shows long range transport of anthropogenically influenced air masses, leading to higher aerosol concentration in the Arctic with especially a BC mass concentration 3 times higher. Thus, March 29<sup>th</sup> constitute the “polluted” case. According to Quennehen et al. (2012), during the route, the Aitken mode concentration quickly decreases by coagulation, for the benefit of the accumulation mode, increasing the average effective diameter. This explains the accumulation mode dominance observed in Figure 11 and the increase of the average DMPS effective diameter, and confirms the strong influence of the lower latitudes emissions during the “polluted” case. On the contrary, the “clean” case shows local sources composed of fresh particles, for at least half the concentration.

583  
584  
585  
586  
587  
588

This long range anthropogenic pollution has also strong influence on cloud properties. Indeed, CCN abilities being mainly due to the aerosol size in the Arctic (Mc Farquhar et al., 2011), accumulation mode dominance leads to higher aerosol effective diameter and higher  $F_a$  values. Combined with higher aerosol concentration, the droplet concentration increases whereas the droplet size decreases meaning, theoretically, that the cloud optical thickness increases.

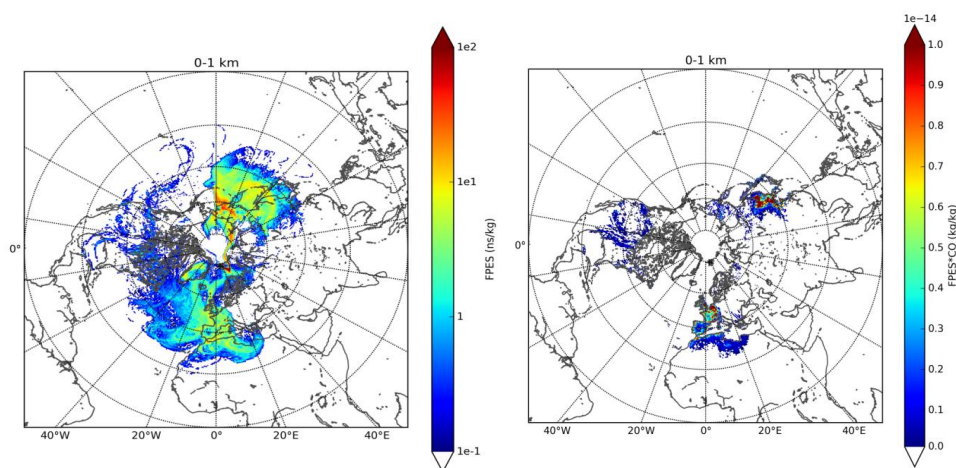


Figure 12: a) and b) Same as Figure 10 for the air masses arriving in the Mount-Zeppelin station on March 29<sup>th</sup> between 10 AM and 1 PM UTC.

589  
 590  
 591  
 592  
 593  
 594  
 595  
 596  
 597

This qualitative study has to be completed with quantitative parameters that can be found in the scientific literature. Therefore, the next section will focus on the quantitative variations of droplet concentration and size according to aerosol properties. Moreover, glaciation and riming indirect effect will be assessed.

#### 598 4.3 Quantification of the impacts of the aerosol properties on the cloud 599 microphysical properties

600  
 601  
 602  
 603  
 604  
 605  
 606

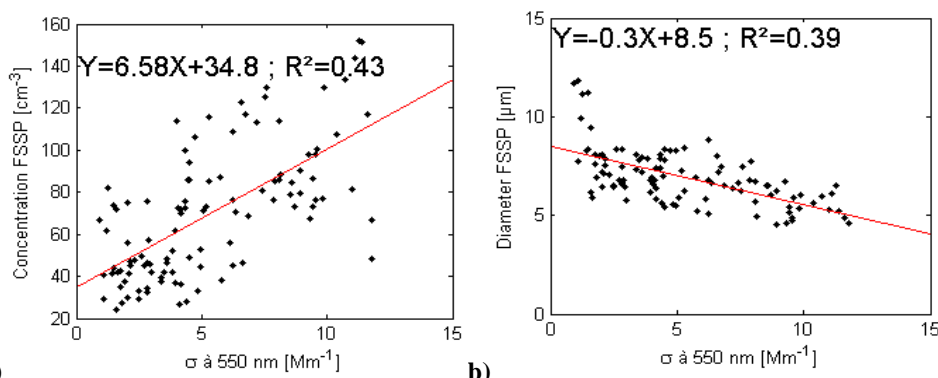
The sensitivity of cloud diameter and concentration according to aerosol haze will be assessed from two parameters, called the Indirect Effect parameter (*IE*) and the Nucleation Efficiency (*NE*) and defined as follows (Feingold et al., 2001, 2003, Garrett et al., 2004):

$$607 \quad IE = - \frac{\partial \ln(r_e)}{\partial \ln(\sigma)} \quad (4)$$

$$608 \quad 609 \quad NE = \frac{\partial \ln(N)}{\partial \ln(\sigma)} \quad (5)$$

610 where  $r_e$  is the droplet effective radius,  $N$  the droplet concentration and  $\sigma$  the aerosol scattering  
 611 coefficient.

612 We made two assumptions to use these parameters. First, *IE* and *NE* are assumed to evaluate  
 613 the variations of the droplet concentration and size according to the CCN concentration. To  
 614 measure this one, we use the scattering coefficient which is assumed to be proportional to the  
 615 CCN concentration. The accumulation mode particles are the most inclined to serve as CCN  
 616 because of their size and possess the highest scattering cross section compared to the other  
 617 modes (Garrett et al., 2004). Second,  $r_e$  and  $N$  are also dependent on the *LWP*, so *IE* and *NE*  
 618 have to be computed for similar *LWP* clouds (Feingold et al., 2001). During CLIMSLIP, the  
 619 *LWP* was not measured and we assumed that the *LWP* is effectively constant. This is reasonable  
 620 since the sampled clouds were all low level mixed phase arctic clouds and from the same season.  
 621

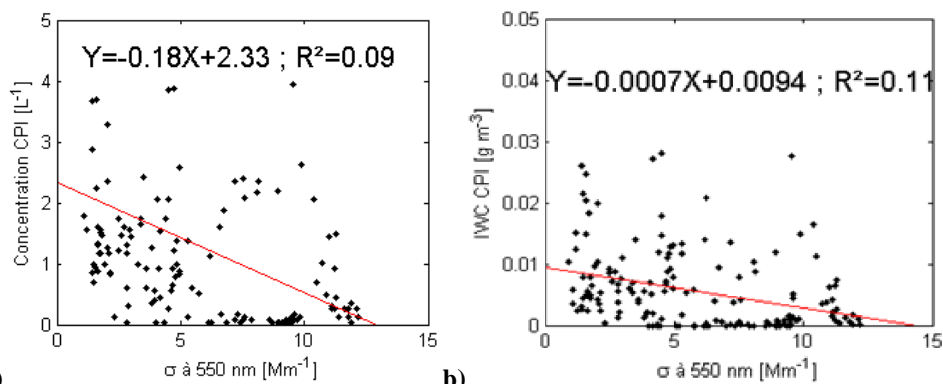


622 **a)**  
 623 **b)**  
 624 Figure 13: Comparison of the aerosol scattering coefficient  $\sigma$  at  $\lambda = 550$  nm measured by the  
 625 nephelometer, with a) the droplet concentration, and b) the effective diameter measured by  
 626 the FSSP, for the four LMPL cases. Values of  $LWC$  below  $5 \cdot 10^{-3} \text{ g m}^{-3}$  were not taken into  
 627 account. This comparison has been performed with a nephelometer time resolution of 5  
 628 minutes.

629 Figure 13 presents the comparisons between the droplet concentration and diameter with the  
 630 aerosol scattering coefficient. The results are consistent with the Twomey effect (Twomey,  
 631 1974, 1977) and the Albrecht effect (Albrecht, 1989). The correlation coefficients  $R^2$  are equal  
 632 to 0.43 and 0.39 for concentration and size, respectively. This high dispersion can be explained  
 633 by the fact that the droplet concentration and size depend also of  $LWP$ , temperature and the  
 634 position of the measurement volume within the cloud system.

635 At  $\lambda = 550$  nm,  $IE = 0.2$  and  $NE = 0.43$  were obtained. This is to compare with the study of  
 636 Garrett et al. (2004) performed at Barrow, Alaska, where  $IE$  and  $NE$  were found to be between  
 637 0.13 and 0.19 and between 0.3 and 0.5 respectively, at  $\lambda = 550$  nm. Very similar values are so  
 638 found in two different regions of the Arctic, which confirms these parameterizations of the first  
 639 and second aerosol indirect effect for the arctic region.

640



641 **a)**  
 642 **b)**  
 643 Figure 14: 5 minutes comparison of the aerosol scattering coefficient  $\sigma$  at  $\lambda = 550$  nm with a)  
 644 the concentration and b) the  $IWC$  of crystals sampled by the CPI, for the four LMPL cases. A  
 645 threshold of  $50 \mu\text{m}$  was applied to the particles diameter to discard the droplets sampled by  
 646 the CPI.  
 647



648 The glaciation (Lohmann, 2002a, 2002b) and the riming indirect effect (Borys et al., 2003) were  
649 evaluated during the CLIMSLIP campaign thanks to the CPI and the nephelometer  
650 measurements. The comparison between the crystal concentration and *IWC* with  $\sigma$  (or nuclei  
651 concentration) is displayed in Figure 14. The results show very weak correlation, for the  
652 concentration and the *IWC*. This means that neither the glaciation nor the riming indirect effect  
653 were revealed during CLIMSLIP.

654 This absence can be due to the high uncertainty in the CPI measurements and/or to low sampling  
655 rate that leads to a very low statistical representation. To compare, the study of Jackson et al.  
656 (2012), during the ISDAC and MPACE campaign, found a correlation corresponding to the  
657 glaciation effect above the cloud liquid phase but no evidence of the riming effect.

658

659

660

661

662

663

664

665

666

667

668

669

670

671

672

673

674

675

676

677

678

679

680

681

682

683

684

685

686

687

688

689

690

691

692

693

694

695



## 696 **5 Summary and conclusion**

697

698 Within the framework of the arctic amplification, the complex interactions between the cloud  
699 and aerosol properties remain a challenge to enhance the arctic cloud modeling and to get a  
700 better quantification of the consequences of the anthropogenic pollution on the arctic climate.  
701 The ANR project CLIMSLIP (CLimate IMPacts of Short-LIved Pollutants in the polar region)  
702 provides new data from a ground based aerosol and cloud instrumentation located at the Mount  
703 Zeppelin station, Ny-Alesund, Svalbard, during spring 2012. This instrumentation contains a  
704 FSSP, a CPI and a Polar Nephelometer to sample clouds and a CPC, a DMPS and a  
705 nephelometer for aerosols.

706 During the campaign, four cases of LMPL (Liquid and Mixed Phase Layer), three cases of snow  
707 precipitation layer and two cases of BS (Blowing Snow) were sampled. The precipitation layer  
708 cases correspond to the lower layer of a MPC. The precipitation events are composed of large  
709 crystals (Mean Diameter  $D_m \sim 350 \mu\text{m}$ ) with an important presence of stellar. The LMPL events  
710 are characterized by a bimodal PSD with a large number of droplets. The liquid mode was  
711 located around  $10 \mu\text{m}$  and the crystal mode around  $250 \mu\text{m}$ . The phase function measurements  
712 showed an increase of the lateral scattering as  $F_{liq}$  decreases.

713 According to Guyot et al. (2015), only isoaxial measurements with a wind speed higher than 5  
714 m/s are selected. This deleted a non-negligible amount of data and so limited the analysis,  
715 especially for the precipitation cases where the particle statistics were the weaker. Moreover,  
716 the position of the station within the cloud system was approximate despite the ceilometer  
717 measurements.

718 A study by comparison of the effects of the anthropological aerosols transported to the Arctic  
719 was performed. According to the FLEXPART/WRF simulations, the “polluted” case of March  
720 29<sup>th</sup> showed air masses from Europe and East Asia whereas the aerosol sources during the  
721 “clean” case of March 11<sup>th</sup> were closer (mainly from Scandinavia) and the anthropogenic  
722 contribution doesn't exceed northern Europe.

723 Thus, the polluted case presents higher Black Carbon, aerosol and droplets concentrations, a  
724 more important accumulation mode, smaller droplet sizes and higher activation fraction  $F_a$ . The  
725 March 29<sup>th</sup> activation diameter  $D_a$  decreased when the droplet diameter increased and  $F_a$   
726 increased, proving that smaller aerosol particles are activated and droplets grow up when the  
727 aerosol number decreases. These results confirm the first and second aerosol indirect effects  
728 with the coefficients  $IE$  and  $NE$  respectively around 0.2 and 0.43. These values are very close  
729 to those found by Garrett et al. (2004), which performed measurement at Barrow in Alaska, and  
730 are so good candidates to be used to parameterize arctic aerosol-cloud interaction in climate  
731 models. Furthermore, the crystal concentration and  $IWC$  do not show any correlation with the  
732 aerosol properties, which indicates that the glaciation and riming indirect effects are not  
733 highlighted during the CLIMSLIP-NyA campaign.

734

735

736 *Acknowledgements.* This work was supported by the ANR project CLIMSLIP and the conseil  
737 general de l'Allier. We also thank the AVI for providing the ceilometer data and the ITM and  
738 NILU for monitoring the Mount Zeppelin station. We are grateful to scientists, engineers and  
739 technicians that make this study possible. Boris Quennehen acknowledges the IPSL  
740 CICALAD/CLIMSERV mesocenter for providing computing resources.

741

742

743

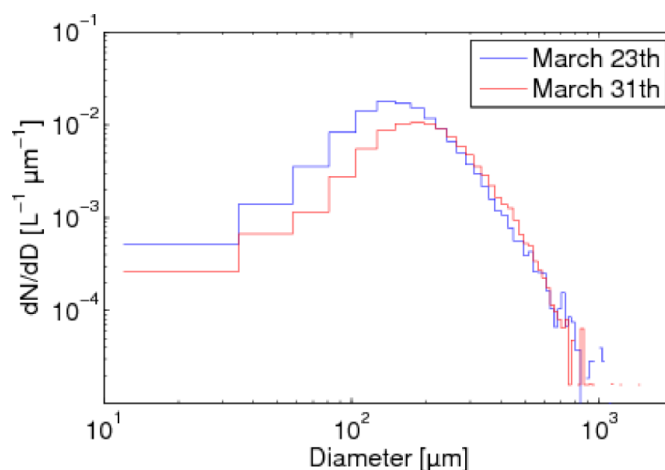
744

745

746 **Annex: Characterization of the Blowing Snow (BS) cases**

747

748 During ground based measurements, some snow was collected that was suspended in the  
749 atmosphere due to wind. This is the so-called Blowing Snow (BS). This annex aims at the  
750 microphysics characterization in order to recognize this kind of episode and the optical  
751 properties measurements, especially the phase function, that can be used as a reference to  
752 develop new parameterizations of the snow simple scattering properties (Räisänen et al., 2015).  
753



754 Figure 15: Same as Figure 5 for the BS cases.

755

756

757

758

759

760

761

762

763

764

765

766

767

768

When the BS occurs, the sky is clear as observed by the ceilometer. However, crystal particles are sampled. They are snowflakes initially resting on the ground but getting suspended in the air by the wind.

Figure 15 shows the average PSDs measured by the CPI for the two BS cases. The shape and the amplitude are similar for the two PSDs, with a mean diameter between 150 and 200  $\mu\text{m}$ . for a maximum class concentration around  $10^{-2} \text{ L}^{-1} \mu\text{m}^{-1}$ . The CPI shape classification, plotted in Figure 16.a, shows a large prevalence of irregular crystals, as well in number, surface or mass (i.e. volume), with a percentage around 90% of the crystals. These two characteristics constitute the microphysics signature of the BS. The difference between the BS and MPC (see Figure 5 and 6) signature makes it possible to identify BS events even if the station is located inside a cloud.



769

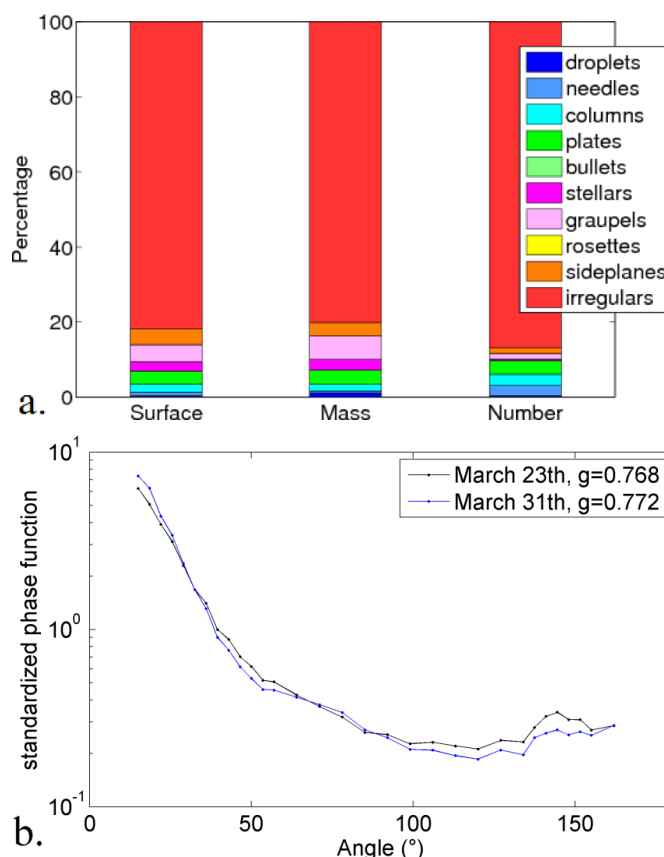


Figure 16: Same as Figure 6 (a and b) for the BS cases.

770

771

772

773

774

775

776

777

778

779

780

781

782

783

784

785

786

787

788

789

790

Even if the resuspension of crystals in the air can modify the shape by impacts, we consider that the sampled crystals are similar to the deposited precipitations and aged for several days. Thus, the BS events during CLIMSLIP were excellent occasions to measure the arctic snow properties.

Figure 16.b displays the average phase functions of the BS cases. The shape of the curves are very similar to the precipitation cases, typical of ice particles, but with lower  $g$  values. These measurements constitute a unique database to develop parameterizations of the arctic snow optical properties. Indeed, in most of the climate and weather forecast models, the computation of the snow albedo uses the approximation of spherical snow grain (Wang and Zeng, 2010). Thus, the study of Räisänen et al. (2015) proposes new modeling parameterizations of the snow single scattering properties (SSP) based on the CLIMSLIP-NyA in situ measurement of the phase function. The obtained snow SSP takes into account the complex BS particles shape (Räisänen et al., 2015).



791 **References**

792

793 Abdul-Razzak, H., Ghan, S. and Rivera-Carpio, C.: A parametrization of aerosol activation; 1.  
794 Single aerosol type, *J. Geophys. Res.*, 103, 6123-6131, 1998.

795

796 Albrecht, B.A.: Aerosols, cloud microphysics, and fractional cloudiness, *Science*, 245, 1227-  
797 1230, 1989.

798

799 Bailey, M. P., and Hallett, J.: A Comprehensive Habit Diagram for Atmospheric Ice Crystals:  
800 Confirmation from the Laboratory, AIRS II, and Other Field Studies, *J. Atmos. Sci.*, 66, 2888-  
801 2899, doi:10.1175/2009JAS2883.1, 2009.

802

803 Baker, B. and Lawson, R.P.: Improvement in Determination of Ice Water Content from Two-  
804 Dimensional Particle Imagery. Part I: Image-to-Mass Relationships. *J. Appl. Meteor. Climatol.*,  
805 45, 1282-1290, 2006.

806

807 Borys, R.D., Lowenthal, D.H., Cohn S.A. and Brown, W.O.J.: Mountaintop and radar  
808 measurements of anthropogenic aerosol effects on snow growth and snowfall rate, *Geophys.*  
809 *Res. Lett.*, 30, 1538, doi:10.1029/2002GL016855, 2003.

810

811 Boucher, O., Randall, D., Artaxo, P., Bretherton, C., Feingold, G., Forster, P., Kerminen, V.-  
812 M., Kondo, Y., Liao, H., Lohmann, U., Rasch, P., Satheesh, S.K., Sherwood, S., Stevens B. and  
813 Zhang, X.Y.: Clouds and Aerosols. In: *Climate Change 2013: The Physical Science Basis.*  
814 Contribution of Working Group I to the Fifth Assessment Report of the Intergovernmental  
815 Panel on Climate Change, Cambridge University Press, Cambridge, United Kingdom and New  
816 York, NY, USA, 2013.

817

818 Brioude, J., Arnold, D., Stohl, A., Cassiani, M., Morton, D., Seibert, P., Angevine, W., Evan,  
819 S., Dingwell, A., Fast, J. D., Easter, R. C., Pisso, I., Burkhardt, J., and Wotawa, G.: The  
820 Lagrangian particle dispersion model FLEXPART-WRF version 3.1, *Geosci. Model Dev.*, 6,  
821 1889-1904, doi:10.5194/gmd-6-1889-2013, 2013.

822

823 Costa, A., Krämer, M., Meyer, J., Afchine, A., Luebke, A., Dorsey, J.R., Gallagher, M.W.,  
824 Ehrlich, A., Wendisch, M., Baumgardner, D., Möhler, O., Saathoff, H. and Schnaiter, M.: A  
825 microphysical classification of mixed-phase clouds in the liquid-ice coexistence and Wegener-  
826 Bergeron-Findeisen regime, 14th Conference on Cloud Physics, 07 – 11 July 2014, Boston,  
827 USA, [https://ams.confex.com/ams/14CLOUD14ATRAD/webprogram/Handout/Paper250419/AMS\\_Poster\\_68\\_Mixed\\_Phase\\_Clouds\\_Costa.pdf](https://ams.confex.com/ams/14CLOUD14ATRAD/webprogram/Handout/Paper250419/AMS_Poster_68_Mixed_Phase_Clouds_Costa.pdf), 2014.

828

830 Curry, J.A., Randall, D., Rossow, W.B., and Schramm, J.L.: Overview of Arctic Cloud and  
831 Radiation Characteristics, *J. Climate*, 9, 1731-1764, doi: 10.1175/1520-  
832 0442(1996)009<1731:OOACAR>2.0.CO;2, 1996.

833

834 Dufresne, J.L. and Bony, S. : An Assessment of the Primary Sources of Spread of Global  
835 Warming Estimates from Coupled Atmosphere–Ocean Models, *J. of Clim.*, 21, 5135 – 5144,  
836 2008.

837

838 Dye, J.E., Baumgardner D.: Evaluation of the Forward Scattering Spectrometer Probe. Part I:  
839 Electronic and Optical Studies, *J. Atmos. Oceanic Technol.*, 1, 329-344, 1984.

840



- 841 Eleftheriadis, K., Vratolis, S. and Nyeki, S.: Aerosol black carbon in the European Arctic:  
842 Measurements at Zeppelin station, Ny-Alesund, Svalbard from 1998–2007, *Geophys. Res.*  
843 *Let.*, 36, L02809, doi:10.1029/2008GL035741, 2009.
- 844
- 845 Engvall, A.C., Krejci, R., Ström, J., Treffeisen, R., Scheele, R., Hermansen, O. and Paatero, J.:  
846 Changes in aerosol properties during spring-summer period in the Arctic troposphere, *Atmos.*  
847 *Chem. Phys.*, 8, 445–462, 2008.
- 848
- 849 Febvre G., Gayet, J.F., Shcherbakov., V., Gourbeyre, C., Jourdan, O.: Some effects of ice  
850 crystals on the FSSP measurements in mixed phase clouds, *Atmos. Chem. Phys.*, 12, 8963–  
851 8977, doi: 10.5194/acp-12-8963-2012, 2012.
- 852
- 853 Feingold, G., Remer, L. A., Ramaprasad, J., and Kaufman, Y. J.: Analysis of smoke impact on  
854 clouds in Brazilian biomass burning regions: An extension of Twomey’s approach, *J. Geophys.*  
855 *Res.*, 106, 22, 907– 22, 922, 2001.
- 856
- 857 Feingold, G., Eberhard, W. L., Veron, D. E. and Previdi, M.: First measurements of the  
858 Twomey indirect effect using ground-based remote sensors, *Geophys. Res. Lett.*, 30, 1287, doi:  
859 10.1029/2002GL016633, 2003.
- 860
- 861 Garrett, T. J., Hobbs, P. V., and Gerber, H.: Shortwave, single scattering properties of Arctic  
862 ice clouds, *J. Geophys. Res.*, 106, 15 155–15 172, 2001.
- 863
- 864 Garrett, T. J., Zhao, C. Dong, X., Mace, G., Hobbs, P. V.: Effects of Varying Aerosol Regimes  
865 on Low-Level Arctic Stratus. *Geophys. Res. Lett.*, 31, 17, 17, doi: 10.1029/2004GL019928,  
866 2004.
- 867
- 868 Garrett, T. and Zhao, C.: Increased Arctic cloud longwave emissivity associated with pollution  
869 from mid-latitudes, *Nature*, 440, 787–789, doi:10.1038/nature04636, 2006.
- 870
- 871 Gayet, J.F., Crépel, O., Fournol, J.F., and Oshchepkov, A.: A new airborne polar nephelometer  
872 for the measurements of optical cloud properties. Part I: Theoretical design, *Ann. Geophysicae*,  
873 15, 451–459, 1997.
- 874
- 875 Gayet, J.F., Auriol, F., Minikin, A., Ström, J., Seifert, M., Krejci, R., Petzol, A., Febvre, G.,  
876 and Schuman, U.: Quantitative measurement of the microphysical and optical properties of  
877 cirrus clouds with four different in situ probes: Evidence of small crystals, *Geo. Resea. Let.*,  
878 29, 2230–2233, 2002.
- 879
- 880 Gayet, J.F., Mioche, G., Dörnbrack, A., Ehrlich, A., Lampert, A., Wendisch M.: Microphysical  
881 and optical properties of Arctic mixed-phase clouds. The 9 April 2007 case study, *Atmos.*  
882 *Chem. Phys.*, 9, 6581–6595, 2009.
- 883
- 884 Guyot, G., Gourbeyre, C., Febvre, G., Shcherbakov, V., Brunet, F., Dupont, J.C., Sellegri, K.  
885 and Jourdan, O.: Quantitative evaluation of seven optical sensors for cloud microphysical  
886 measurements at the Puy-de-Dôme Observatory, France, *Atmos. Meas. Tech.*, 8, 4347–4367,  
887 doi:10.5194/amt-8-4347-2015 , 2015.
- 888
- 889 Jackson, R.C., McFarquhar, G.M., Korolev, A.V., Earle, M.E., Liu, P.S.K., Lawson, R.P.,  
890 Brooks, S., Wolde, M., Laskin, A. and Freer, M. : The dependence of ice microphysics on



- 891 aerosol concentration in arctic mixed-phase stratus clouds during ISDAC and M-PACE, J.  
892 Geophys. Res., 117, D15207, doi:10.1029/2012JD017668, 2012.  
893
- 894 Jourdan, O., Mioche, G., Garrett, T.J., Schwarzenböck, A., Vidot, J., Xie, Y., Shcherbakov, V.,  
895 Yang, P. and Gayet, J.F.: Coupling of the microphysical and optical properties of an Arctic  
896 nimbostratus cloud during the ASTAR 2004 experiment: Implications for light- scattering  
897 modeling, J. Geophys. Res., 115, D23206, doi:10.1029/2010JD014016, 2010.  
898
- 899 Kay, J. E., Holland, M. M., Bitz, C. M., Blanchard-Wrigglesworth, E., Gettelman, A., Conley,  
900 A. and Bailey, D.: The Influence of Local Feedbacks and Northward Heat Transport on the  
901 Equilibrium Arctic Climate Response to Increased Greenhouse Gas Forcing, J. Clim., 25(16),  
902 5433–5450, doi:10.1175/JCLI-D-11-00622.1, 2012.  
903
- 904 Klimont, Z., Kupiainen, K., Heyes, C., Purohit, P., Cofala, J., Rafaj, P., Borcken-Kleefeld, J.,  
905 and Schöpp, W.: Global anthropogenic emissions of particulate matter including black carbon,  
906 Atmos. Chem. Phys. Discuss., <https://doi.org/10.5194/acp-2016-880>, in review, 2016.  
907
- 908 Knollenberg, R.G.: Techniques for probing cloud microstructure, in: Clouds, their formation,  
909 optical properties and effects, Hobbs, P.V. and Deepak, A., Academic Press, New York, USA,  
910 15-92, 1981.  
911
- 912 Korolev, A.V., Strapp, J.W., Isaac, G.A. et Nevzorov, A.N.: The Nevzorov airborne hot wire  
913 LWC-TWC probe: Principe of operation and performance characteristics, J. Atmos. Ocean.  
914 Techn., 15, 1495-1510, 1998.  
915
- 916 Korolev, A. V. and Isaac, G. A., Relative humidity in liquid, mixed-phase, and ice clouds, J.  
917 Atmos. Sci., 63, 2865–2880, 2006.  
918
- 919 Lawson, R.P. and Baker, B.: Improvement in Determination of Ice Water Content from Two-  
920 Dimensional Particle Imagery. Part II: Applications to Collected Data. J. Appl. Meteor.  
921 Climatol., 45, 1291–1303, 2006.  
922
- 923 Lefèvre, R. : Physique de la mesure de la sonde CPI pour la mesure des propriétés des cristaux  
924 de glace. Application aux observations réalisées durant la campagne ASTAR 2004, 186 p.,  
925 Manuscrit de thèse, Université Blaise Pascal, 2007.  
926
- 927 Lohmann, U.: Possible Aerosol Effects on Ice Clouds via Contact Nucleation, J. Atmos. Sci.,  
928 59, 647–656, , 2002a.  
929
- 930 Lohmann, U.: A glaciation indirect aerosol effect caused by soot aerosols, Geophys. Res. Lett.,  
931 29, 1052-1056, doi:10.1029/2001GL014357, 2002b.  
932
- 933 Mc Farquhar, G., Ghan, S. J., Verlinde, J., Korolev, A., Strapp, J. W., Schmid, B., Tomlinson,  
934 J., Wolde, M., Brooks, S., Cziczo, D., Dubey, M., Fan, J., Flynn, C., Gultepe, I., Hubbe, J.,  
935 Gilles, M., Laskin, A., Lawson, P., Leaitch, W., Liu, P., Liu, X., Lubin, D., Mazzoleni, C., Mac  
936 Donald, A.M., Mo\_et, R., Morrison, H., Ovchinnikov, M., Shupe, M., Turner, D., Xie, S.,  
937 Zelenyuk, A., Bae, K, Freer, M., and Glen, A.: Indirect and semi-direct aerosol campaign: the  
938 impact of Arctic aerosols on clouds, B. Am. Meteorol. Soc., 92, 183–201,  
939 doi:10.1175/2010BAMS2935.1, 2011.  
940



- 941 Mc Guire, D., Chapin, F.S., Walsh, J., Wirth, C.: Integrated regional changes in arctic climate  
942 feedbacks: Implications for the Global Climate System, *Annu. Rev. Environ. Resour.*, 31, 61–  
943 91, doi: 10.1146/annurev.energy.31.020105.100253, 2006.
- 944
- 945 Mioche, G., Jourdan, O., Ceccaldi, M., and Delanoë, J.: Variability of mixed-phase clouds in  
946 the Arctic with a focus on the Svalbard region: a study based on spaceborne active remote  
947 sensing, *Atmos. Chem. Phys.*, 15, 2445–2461, doi:10.5194/acp-15-2445-2015, 2015.
- 948
- 949 Morrison, H., de Boer, G., Feingold, G., Harrington, J., Shupe, M.D., and Sulia, K.: Resilience  
950 of persistent Arctic mixed-phase clouds, *Nat. Geosci.*, 5, 11–17, doi:10.1038/ngeo1332, 2012.
- 951
- 952 Pincus, R. and Baker, M.: Effect of precipitation on the albedo susceptibility of clouds in the  
953 marine boundary layer, *Nature*, 372, 250 – 252, doi: 10.1038/372250a0, 1994.
- 954
- 955 Quennehen, B., Schwarzenboeck, A., Matsuki, A., Burkhart, J. F., Stohl, A., Ancellet, G., and  
956 Law, K. S.: Anthropogenic and forest fire pollution aerosol transported to the Arctic:  
957 observations from the POLARCAT-France spring campaign, *Atmos. Chem. Phys.*, 12, 6437–  
958 6454, doi:10.5194/acp-12-6437-2012, 2012.
- 959
- 960 Quinn, P. K., Shaw, G.E. Andrews, E., Dutton, E.G., Ruoho-Airola, T. and Gong, L.: Arctic  
961 haze: current trends and knowledge gaps, *Tellus*, 59, 99–114, 2007.
- 962
- 963 Quinn, P. K., Bates, T. S., Baum, E., Doubleday, N., Fiore, A. M., Flanner, M., Fridlind, A.,  
964 Garrett, T. J., Koch, D., Menon, S., Shindell, D., Stohl, A., and Warren, S. G.: Short-lived  
965 pollutants in the Arctic: their climate impact and possible mitigation strategies, *Atmos. Chem.*  
966 *Phys.*, 8, 1723–1735, doi:10.5194/acp-8-1723-2008, 2008.
- 967
- 968 Räisänen, P., Kokhanovsky, A., Guyot, G., Jourdan, O., Nousiainen, T.: Parameterization of  
969 single-scattering properties of snow, *The Cryosphere*, 9, 1277–1301, doi:10.5194/tc-9-1277-  
970 2015, 2015.
- 971
- 972 Rogers, D., Stith, J., Jensen, J., Cooper, W., Nagel, D., Maixner, U. and Goyea, O.: Splash  
973 artifacts in FSSP measurements; observations and flow modeling studies, 12th conference of  
974 cloud physics, Madison, USA, 10 – 14 July 2006, P2.30, 2006.
- 975
- 976 Screen, J.A. and Simmonds, I.: The central role of diminishing sea ice in recent Arctic  
977 temperature amplification, *Nature*, 464, 1334–1337, doi:10.1038/nature09051, 2010.
- 978
- 979 Serreze, M. and Francis, J.: The arctic amplification debate, *Climatic Change*, 76, 241 – 264,  
980 doi: 10.1007/s10584-005-9017-y, 2006.
- 981
- 982 Skamarock, W. C., J. B. Klemp, J. Dudhia, D. O. Gill, D. M. Barker, M. G Duda, X.-Y. Huang,  
983 W. Wang, and J. G. Powers, 2008: A Description of the Advanced Research WRF Version 3.  
984 *NCAR Tech. Note NCAR/TN-475+STR*, 113 pp.,  
985 doi:10.5065/D68S4MVH, 2008.
- 986
- 987 Stohl, A., Hittenberger, M. and Wotawa, G.: Validation of the Lagrangian particle dispersion  
988 model FLEXPART against large scale tracer experiments, *Atmos. Environ.*, 32, 4245–4264,  
989 1998.
- 990



- 991 Stohl, A. and Thomson, D.J.: A density correction for Lagrangian particle dispersion models,  
992 Bound.-Layer Met., 90, 155-167, 1999.  
993
- 994 Stohl, A., Forster, C., Frank, A., Seibert, P. and Wotaw, G.: Technical Note: The Lagrangian  
995 particle dispersion model FLEXPART version 6.2, Atmos. Chem. Phys., 5, 2461-2474, 2005.  
996
- 997 TSI: Model 3025A Ultrafine Condensation Particle Counter Instruction Manual, 2002.  
998
- 999 TSI: Model 3563 Integrating Nephelometer Operation and Service Manual, 219 pp, 2005.  
1000
- 1001 Tunved, P., Ström, J. and Krejci, R.: Arctic aerosol life cycle: linking aerosol size distributions  
1002 observed between 2000 and 2010 with air mass transport and precipitation at Zeppelin station,  
1003 Ny-Alesund, Svalbard, Atmos. Chem. Phys., 13, 3643–3660, doi:10.5194/acp-13-3643-2013,  
1004 2013.  
1005
- 1006 Twomey, S.: Pollution and the planetary albedo, Atmos. Environ., 8, 1251 – 1256, 1974.  
1007
- 1008 Twomey, S.: The influence of pollution on the shortwave albedo of clouds, J. of Atmos.  
1009 Sciences, 34, 1149 – 1152, 1977.  
1010
- 1011 Uchiyama, A., Yamazaki, A., Shiobara, M. and Kobayashi, H. : Case study on microphysical  
1012 properties of boundary layer mixed-phase cloud observed at Ny-Ålesund, Svalbard: Observed  
1013 cloud microphysics and calculated optical properties on 9 June 2011, Polar Science, 8(2), 57–  
1014 72, doi:10.1016/j.polar.2013.11.001, 2013.  
1015
- 1016 Vaughan, D.G., Comiso, J.C., Allison, I., Carrasco, J., Kaser, G., Kwok, R., Mote, P., Murray,  
1017 T., Paul, F., Ren, J., Rignot, E., Solomina, O. Steffen, K. and Zhang, T.: Observations:  
1018 Cryosphere. In: Climate Change 2013: The Physical Science Basis. Contribution of Working  
1019 Group I to the Fifth Assessment Report of the Intergovernmental Panel on Climate Change  
1020 [Stocker, T.F., D. Qin, G.-K. Plattner, M. Tignor, S.K. Allen, J. Boschung, A. Nauels, Y. Xia,  
1021 V. Bex and P.M. Midgley (eds.)]. Cambridge University Press, Cambridge, United Kingdom  
1022 and New York, NY, USA, 2013.  
1023
- 1024 Wang, Z. and Zeng, X.: Evaluation of snow albedo in land models for weather and climate  
1025 studies, J. Appl. Meteorol. Clim., 49, 363–380, 2010.  
1026
- 1027 Wendisch, M., Yang, P., and Ehrlich, A.: Amplified climate changes in the Arctic: Role of  
1028 clouds and atmospheric radiation, vol. 132, 1–34, Sitzungsberichte der Sächsischen Akademie  
1029 der Wissenschaften zu Leipzig, Mathematisch-Naturwissenschaftliche Klasse, S. Hirzel  
1030 Verlag, Stuttgart/Leipzig, 2013.